Cubic Anisotropy for a Reconfigurable Magnonic Crystal Based on Co$_2$MnSi Heusler Alloy

S. Mantion and N. Biziere[*]

CEMES, Université de Toulouse, CNRS, UPS, 29 rue Jeanne Marvig, F-31055 Toulouse, France

We explore the possibility offered by magnetic materials with cubic anisotropy to realize reconfigurable magnonic crystals with a very simple geometry working at zero magnetic field. As a proof of concept, we use micromagnetic simulations to calculate the static and dynamic magnetic configurations of a squared antidot lattice made with Co$_2$MnSi Heusler alloy having an anisotropy constant of about 17×10^3 J/m^3. We show that the cubic anisotropy allows very different magnetic states to be obtained at remanence as a function of the direction of a saturation magnetic field, including quasiuniform remanent states that cannot be obtained in materials with the same magnetic parameters but without crystal anisotropy. This leads to the possibility to excite or extinct several quantized spin-wave modes whose frequencies can be tuned with the antidot dimensions. Reconfigurable magnetic states are demonstrated for antidot sizes in the range 300–350 nm for a ratio between the antidot size and spacing equal to 1/3. The transition between two different remanent states can be obtained with low-amplitude magnetic field (down to 3.5 mT) and with a switching time faster than 1 ns, which is of great interest for applications. Oppositely, for a particular orientation of the antidot lattice with respect to the cubic anisotropy axes, we also obtain a single stable remanent state independent of the saturation field direction. Finally, propagation properties and frequency band gaps in an antidot lattice with lateral antidot size of 100 nm are studied for frequency-filtering applications at remanence. Both magnetostatic surface waves and magnetostatic backward-volume wave configurations are explored for different positions of the microwave excitation with respect to the magnonic crystal.

I. INTRODUCTION

Magnonics is a very active field in magnetism consisting of manipulating the amplitude or phase of spin waves to achieve logical operations and communication technologies [1,2]. In particular, the very small wavelength of spin waves in the microwave range (from few nm up to few μm) and their frequency tuning with external magnetic fields allow exploration of the miniaturization of microwave to subterahertz devices for on-chip integration. This makes magnonics a promising alternative for post-CMOS technology and many applications of spin-wave-based devices have already been demonstrated [2–6].

In this field, magnonic crystals (MCs) play a major role. They consist of a magnetic material with a periodic modulation of one or several magnetic parameters (magnetization, anisotropy). These metamaterials are the magnetic counterpart of photonic crystals. Due to the periodic lattice, forbidden frequency band gaps for spin-wave propagation appear. Recent developments in MCs have focused on reconfigurable devices. Such systems aim at getting multiple remanent states, thus allowing different microwave responses, without the need for a bias field that

limits chip integration. In addition to logical and communication devices, MCs are very attractive to develop innovating passive microwave devices such as filters, circulators, receivers, etc.

Applications also require a simple initialization scheme with low energy consumption and a fast initialization time. Very interesting routes have been explored to fulfil these requirements such as dipolar-coupled nanowires and nanopillars [7,8], current-induced Oersted field [9,10], laser heating [11,12], spin ice [13], or voltage-controlled hybrid multiferroic-ferromagnetic material [14]. Among these promising routes, recent studies focussed on the use of shape anisotropy, in particular, geometries such as arrays of rhomboid [15], trapezoidal [16], L- and C-shape nanomagnets [17]. In such systems, the transition between different remanent magnetic states is stabilized through the dipolar coupling between the elements. Furthermore, the transition between the states is predicted to be very fast (below 1 ns) but obtained with a relatively large applied field (few tens of mT).

Beside these achievements, it appears that considering the intrinsic magnetic material properties and, in particular, the crystal anisotropy of magnetic material has been poorly considered so far to make reconfigurable devices. In the case of sufficiently strong cubic anisotropy, it is

*[*]nicolas.biziere@cemes.fr

possible to obtain different remanent magnetic configurations, including quasiuniform states, after application of a saturation field in different directions. Among the different cubic anisotropy materials, Co_2MnSi Heusler alloys can be of particular interest. They have a high Curie temperature (approximately equal to 900 K) allowing high thermal stability for applications [18]. Reported experimental values of saturation magnetization M_s and cubic anisotropy constant K are relatively high ($\mu_0 M_s$ up to 1.3 T and K up to 17×10^3 J/m^3) [19–22]. This allows high-frequency applications in the gigahertz (GHz) range. In addition, a very low Gilbert-type damping constant down to 7×10^{-4} has been measured with a high spin polarization $P = 93\%$ [23,24]. Low damping materials are required for devices that need a long spin-wave propagation distance. For all these reasons, Co_2MnSi has been one of the most studied Heusler alloys in the past 15 years but other Co_2YZ compounds are extremely interesting for applications [24–29].

Here we discuss the possibility to obtain reconfigurable magnonic properties in a simple and classical squared antidot geometry with a crystal of Co_2MnSi Heusler alloy as a model system. Simulations show that the switching between different remanent states can be obtained in about 1 ns with a magnetic field pulse of few mT. The calculated confined spin-wave mode frequencies show an almost complete extinction of several particular modes as a function of the applied field direction for particular values of the ratio between the antidot size and their spacing. We demonstrate that this effect can be reliable for antidot sizes as small as 50 nm. We compare these results with the ones that could be obtained for a material without crystal anisotropy. In addition, we show that a 45° rotation of the antidot lattice with respect to the cubic anisotropy axes allows retrieving always the same microwave response independently of the direction of an applied field. Such behavior can be interesting for applications where the microwave properties must be stable against magnetic perturbations. Finally, we discuss the propagation properties of magnetostatic surface waves (MSSWs) and magnetostatic backward-volume waves (MSBVWs) through an antidot MC in the particular case of an antidot size of 100 nm separated by 300 nm.

II. METHODS

We used Mumax3 [30] to perform micromagnetic simulations of the remanent magnetic states and dynamic spin-wave modes in squared antidot lattices as shown in Fig. 1(a). Mumax3 solves the Landau-Lifshitz equation where the effective field is defined as the sum of the applied external field, the Heisenberg exchange interaction field, the magnetostatic field coming from the shape of the sample and the cubic anisotropy field. The full description of the different terms is given in Ref. [30].
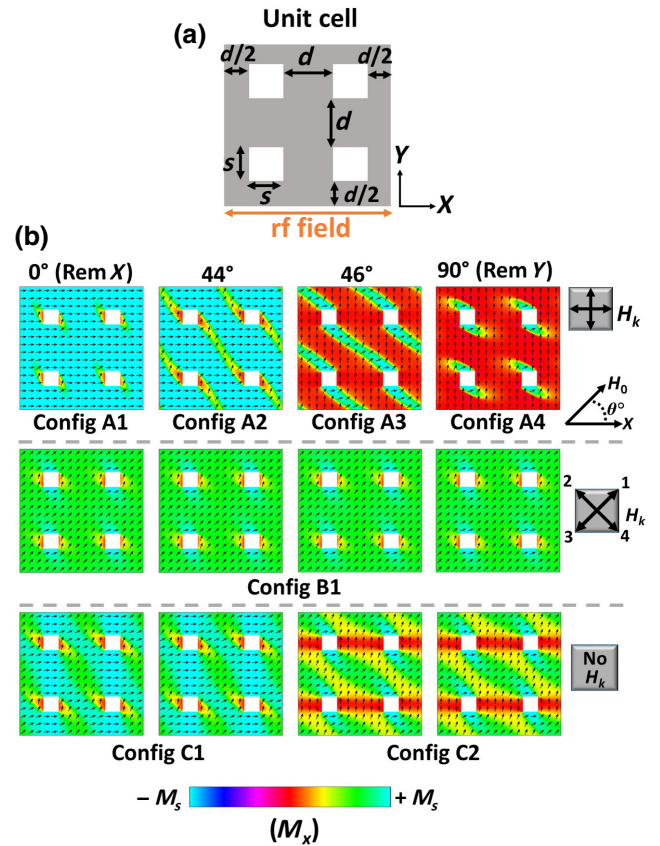

FIG. 1. (a) Schematic of the unit cell for the micromagnetic simulations of the MC. s is the value of the lateral dimensions of the squares and d is the spacing between them. (b) Remanent states as a function of the angle θ between the saturation field H_0 and the X axis for $s = 300$ nm and $d = 900$ nm. The gray squares beside each row show the orientation of the cubic anisotropy axes denoted as H_k (black arrows) in the Co_2MnSi thin film. The first row corresponds to a parallel alignment of the square lattice with H_k, the second row corresponds to a 45° rotation of the square lattice with respect to H_k and the third row corresponds to the remanent states obtained without crystal anisotropy field.

The square antidot size is s and the spacing between the squares is d. We use cubic cells with dimensions $5 \times 5 \times 5$ nm^3, below the exchange length $l_{ex} = \sqrt{2A/\mu_0 M_s^2} \approx 5.4$ nm as defined in Ref. [30]. The magnetic parameters used are the saturation magnetization $M_s = 1003 \times 10^3$ A/m, the exchange constant $A = 18 \times 10^{-12}$ J/m, the cubic anisotropy constant $K = 17 \times 10^3$ J/m^3 ($\mu_0 H_k \approx 35$ mT) and the gyromagnetic ratio $\gamma = 28.7$ GHz/T. Those values are the ones that we obtain experimentally in our previous experiments for chemically ordered L2$_1$ Co_2MnSi [19]. The Gilbert-damping coefficient is set to 1×10^{-3}, in agreement with our findings and recent reported values [22,25,31] below the 10^{-3} range. The film thickness is 20 nm. We use two-dimensional (2D) periodic boundary conditions (PBCs) in order to simulate an infinite MC. All results presented

here are obtained for a unit cell of the MC with lateral dimensions $= (2s + 2d)$. As discussed below, we verify the validity of these calculations for systems with dimensions as large as $30\,000 \times 30\,000 \times 20$ nm^3. Nevertheless, such large simulations require large computer resources and calculation times that cannot allow numerous tests.

For the simulation of the static remanent states, we start with a random orientation of the magnetization and then we apply a 1-T saturation field $\mu_0 H_0$. The field is then decreased in many steps down to zero. Also, we apply the field with a 0.1° misalignment with the symmetry axes (X or Y, for example) of the system. These precautions avoid calculation of metastable remanent states due to the cubic symmetry of the cells. Once the equilibrium

state is reached, the system is left to relax for 10 ns. This defines the initial remanent state for the dynamic simulations. To calculate the frequencies of the spin-wave modes, we apply a uniform magnetic pulse along the X axis of the system. This can mimic a ferromagnetic resonance (FMR) experiment, for example. We apply a magnetic field pulse with a temporal Sinc function such as $h_{rf}(\tau) = \mu_0 h_p \mathrm{Sin}(2\pi f_c(\tau - \tau_{\mathrm{wait}}))/2\pi f_c(\tau - \tau_{\mathrm{wait}})$, where $\mu_0 h_p = 2$ mT is the amplitude, $f_c = 30$ GHz the cutoff frequency, τ the simulation time and $\tau_{\mathrm{wait}} = 5.12$ ns. This method allows excitation of all spin-wave modes that can couple to a uniform microwave field up to the cutoff frequency. We then record 4096 magnetization files every 10 ps. This leads to a Nyquist frequency of 50 GHz. A fast Fourier
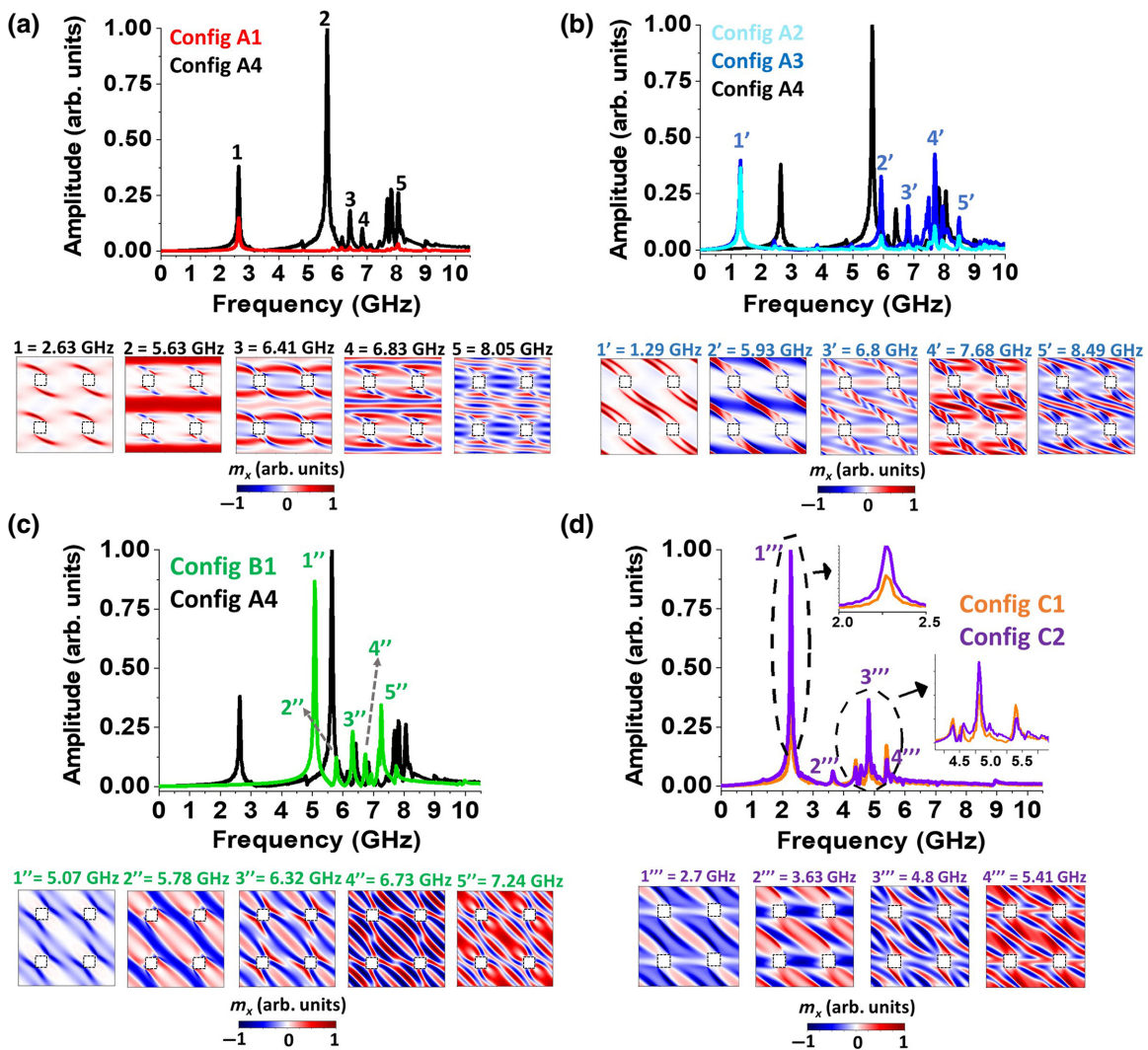

FIG. 2.   FFT amplitude spectra for the different remanent magnetic configurations presented in Fig. 1(a). In (a), (b), and (c), the amplitude of the FFT are normalized with respect to the amplitude of mode 2 in the A4 state. In (d) the amplitude is normalized with respect to the amplitude of mode 1′′′ in the C2 state. Below each FFT, we show temporal snapshots of the dynamic m_x component at the frequencies of the modes indexed in the FFT spectra. The snapshots correspond to the profile at which the amplitude in the central cell of the MC is maximum.
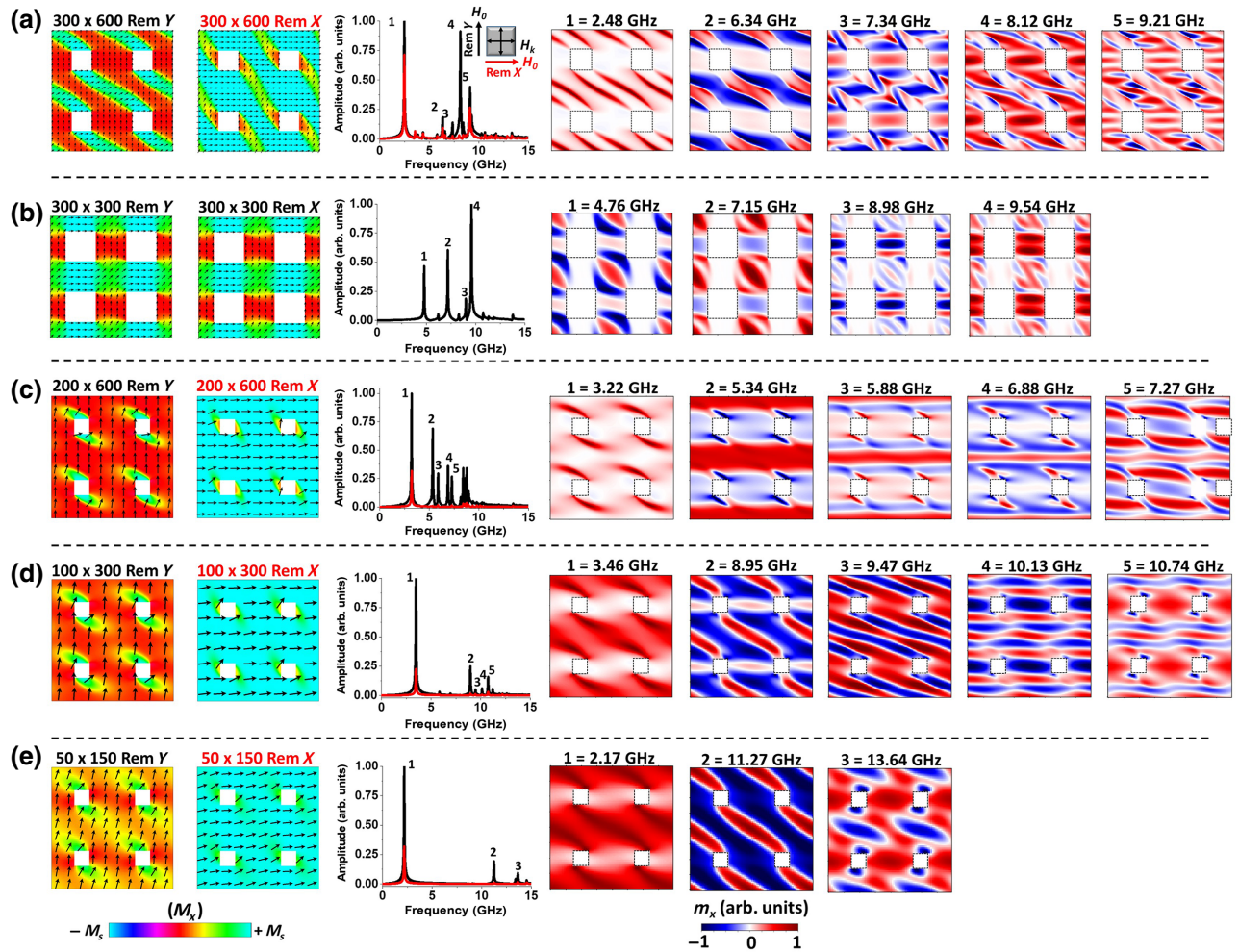
FIG. 3. Remanent magnetic states, FFT spectra and m_x temporal snapshots for different values of s and d. (a) $s = 300$ nm, $d = 600$ nm, (b) $s = 300$ nm, $d = 300$ nm, (c) $s = 200$ nm, $d = 600$ nm, (d) $s = 100$ nm, $d = 300$ nm, (e) $s = 50$ nm, $d = 150$ nm. For all simulations, the antidot lattice is aligned with the cubic anisotropy axis. The m_x profiles are given for the modes indexed in the different FFT spectra. Each FFT spectrum is normalized with respect to the most intense mode. The Rem X and Rem Y remanent states correspond to a saturation field H_0 applied in the X or Y direction, respectively.

transform (FFT) is performed on the time-varying Z component of the magnetization $M_z(\tau)$, averaged over all cells to obtain the frequencies of the spin-wave modes.

To recover the spin-wave profiles, we first subtract the initial equilibrium remanent state to each temporal magnetic file. Then, FFT and inverse FFT are performed to filter a particular frequency and recover the corresponding time evolution of the dynamic m_x component for each cell. The spin-wave profiles shown in Figs. 2 and 3 correspond to the snapshots at the time for which the amplitude of the $m_x(\tau)$ component in the central cell is maximum.

III. RESULTS

We first study a MC with $s = 300$ nm and $d = 900$ nm. Such dimensions are relatively easy to achieve with classical e-beam lithography techniques to make a real device.

Figure 1(b) presents the simulated remanent states as a function of the angle θ between the saturation field H_0 and the X axis. The first row corresponds to the Co$_2$MnSi MC with the antidot lattice aligned along the cubic anisotropy axes denoted as H_k in Fig. 1.

Four remanent magnetic configurations can be obtained. The A1 and A4 configurations correspond to quasiuniform states with most of the magnetization aligned along the direction of H_0 while very small domains appear close to the antidot edges. We refer to these domains as edge domains. They appear to tilt the magnetization in the direction of the local shape anisotropy. The configurations A1 and A4 appear for $0° \leq \theta \leq 40°$ and $50° \leq \theta \leq 90°$, respectively. For the range $40° \leq \theta \leq 50°$, a domain with the magnetization aligned roughly at $45°$ from the X axis appears connecting antidots aligned along the diagonal. We refer to these domains as $45°$ domains. The configurations A2

and A3 differ only by the direction of the magnetization between the 45° domains, depending on the direction of H_0 above or below 45°. Let us note that the configurations A2 or A3 are metastable states in the sense that the lowest energy configurations at remanence are the A1 or A4 states. The A2 or A3 configurations appear when H_0 decreases down to about 8 mT. For this value, the local demagnetizing field combined with the crystal anisotropy field induces a rotation of the magnetization in the X (or Y) direction, between the antidots. However, in the central part of the unit cell, the Zeeman field is still sufficiently strong to stabilize the magnetization at 45°. This configuration remains stable as H_0 is further decreased down to 0 mT.

Figure 2(a) presents the microwave spectrum for the configurations A1 and A4 under a uniform microwave pumping field h_{rf} in the X direction. The amplitudes of the FFT spectra are normalized with respect to the amplitude of the main mode (mode 2 here) in the A4 configuration. Several modes appear with frequencies up to about 10 GHz. Below the graph we show snapshots of the dynamic m_x component for the five modes indexed in Fig. 2(a) for the A4 configuration. The lowest frequency mode corresponds to the dynamic excitation of the edge domains. These localized modes show a relatively large amplitude. Edge-domain modes generally appear at low frequencies as the local effective field is lowered by the competition between the local demagnetizing and exchange fields.

Mode 2 corresponds to a uniform precession of the magnetization in the form of stripes along the X direction between the antidots. More particularly, the volume where the magnetization oscillates is restricted in the vertical direction by the edge domains. The width of these pseudostripes are then about 450 nm, i.e., about half of the nominal spacing between the antidots. We refer to this mode as a quasiuniform stripe mode, in reference to the uniform precession mode observed in uniformly magnetized stripes [32,33]. However, as we can observe, the analogy is not completely true as in our case we also observe a strong magnetization precession inside the edge domain, with the presence of a node in the middle. Mode 3 is mainly related to the magnetic precession in the region between antidots aligned horizontally. Finally, modes 4 and 5 correspond to quantized spin-wave modes in the pseudostripes with a quantification of the wave vector along the Y direction for mode 4 and along both X and Y for mode 5.

As expected for reconfigurable operations, the spectrum in the configuration A1 shows a clear difference with the one of A4. This is because most of the magnetization is aligned with the microwave pumping field, avoiding a direct coupling (as long as the power do not exceed a threshold related to Suhl instabilities [34,35]). In particular, the main mode number 2 is almost extinct. To

give an order of magnitude, we calculate the attenuation of the different modes in dB as $20 \log(M_z^{A1}/M_z^{A4})$. This convention is used because FMR experiments generally refer to the absorbed microwave power, which is proportional to the square of the dynamic magnetization component. For mode 2, the attenuation is about -40 dB. For mode 1, it is only about -10 dB. This is because the magnetization in the edge domains in the configurations A4 and A1 always shows a non-null averaged M_y component that can couple with h_{rf}. For modes 3, 4, and 5, the attenuation is between -20 and -30 dB.

We also compare the amplitude of the FFT spectrum obtained in configuration A4 with the one obtained in configurations A2 and A3 [Fig. 2(b)]. Due to the presence of the 45° domains, we do not have quasiuniform stripe modes anymore. In contrast, the snapshots of the spin-wave profiles show that most of the modes imply a strong dynamic precession inside the 45° domains with an increasing number of nodes and antinodes as the frequency increases. Regarding the reconfigurable microwave functionalities, the possibility to create 45° domains on purpose offers extra functionalities to the device. In particular, it allows obtaining a low-frequency mode 1′, with a frequency shift of 1.3 GHz with respect to mode 1 in the A4 configuration. This leads to an attenuation of -34 dB of mode 1 when switching between mode A4 and A2 or A3. Therefore, this device offers many possibilities depending on the direction of H_0 for on and off switching of several spin-wave modes at well-defined frequencies, with strong amplitude attenuation, in the 1–10 GHz range.

We also test a configuration that could be useful for microwave applications where a constant response independent of external magnetic perturbations is required. This configuration is noted B1 and is shown in the second row of Fig. 1(b). Here, the square lattice is rotated by 45° with respect to the cubic anisotropy axes of the Co_2MnSi thin film. As can be seen, the remanent states are always the same for $0° \leq \theta \leq 90°$. It is quasiuniform across the sample and the magnetization is aligned along the direction of one of the anisotropy axis. The magnetization can be aligned in the direction 1, 2, 3, or 4 depending on the quadrant [second row of Fig. 1(b)] in which H_0 is applied. The main interest here is that all four directions will give a similar microwave spectrum because the averaged M_x and M_y components have always the same absolute magnitude. Figure 2(c) presents the microwave spectrum in configuration B1 and the spin-wave profiles of the first five modes. As compared with configuration A4, the edge-domain mode disappears and the first dynamic mode is around 5 GHz. This one corresponds somehow to a quasiuniform stripe mode but with the stripe aligned along the diagonal of the sample. More generally, it can be observed that all modes are spreading along the diagonal of the sample, with an increasing number of nodes and

antinodes in the direction of the equilibrium magnetization as the frequency increases.

Finally, in order to demonstrate the advantage of materials with crystal cubic anisotropy, we study the expected static and dynamic configurations in the same material but with $K = 0$ (no anisotropy). For every θ value, complex nonuniform remanent states appear, as shown in the third row of Fig. 1(b). In particular, domains with the magnetization aligned at 45° with the X axis always appear in the central part of the unit cell. Configuration C1 is obtained for $0° \leq \theta \leq 45°$ and C2 for $45° \leq \theta \leq 90°$. All spin-wave profiles shown in Fig. 2(d) show a strong precession of the 45° domains. As they are present for the two configurations C1 and C2, attenuation values of the different modes are relatively weak. The maximum attenuation is obtained for the main mode $1'''$ and is about −6 dB only, far from the −40 dB that can be obtained with cubic anisotropy.

IV. INFLUENCE OF THE ASPECT RATIO *s/d*

We now study the reconfigurable properties of the MC as a function of the s and d values. This is mandatory to understand how to design a device that will operate in the desired frequency range.

We first study the influence of the aspect ratio while keeping $s = 300$ nm. When reducing the spacing between the antidots, quasiuniform remanent states cannot be obtained anymore. For $s/d = 1/2$ we observe in Fig. 3(a) that 45° domains form between antidots aligned diagonally. The magnetization in the other parts of the sample aligns either in the X or Y direction depending if θ is below or above 45°, respectively. The two possible remanent states are then written as Rem X and Rem Y, respectively. The profiles of the first five modes in the Rem Y configuration show very complex internal structures, mainly related to the 45° domains' oscillation. The lowest frequency mode appears to be the most intense. It corresponds to a domain-wall resonance at the boundary between the 45° domains and the area where the magnetization is parallel to the X or Y direction. Such domain-wall resonance appears for both Rem X and Rem Y. Therefore, its attenuation is only of −3 dB, which is not relevant for reconfigurable operations. If the mode number 4 shows about −30 dB attenuation, the other modes do not reach −20 dB and such an aspect ratio does not offer performances as good as for $s/d = 1/3$.

For $s/d = 1$, the Rem X and Rem Y states are exactly the same and no reconfigurable operations can be achieved [Fig. 3(b)]. The magnetization rotates toward the X (Y) axis between two vertical (horizontal) antidots to minimize the magnetostatic energy that increases when decreasing d. As a consequence, the area between vertical antidots show almost no coupling with h_{rf} because the magnetization is aligned along X, and the magnetization precession

is localized in the central part of the unit cell and between horizontal antidots. Therefore, decreasing the antidot spacing for a constant value of s tends to reduce the attenuation values of the spin-wave modes because of the impossibility to reach quasiuniform remanent states. For the magnetic parameters of Co_2MnSi alloy used in this study, an aspect ratio $s/d = 1/3$ is suitable to ensure reconfigurable MC. However, this ratio will depend on the material parameters and especially on the cubic anisotropy, exchange, and saturation magnetization constants.

While keeping the ratio $s/d = 1/3$, we study the evolution of the microwave spectra and spin-wave modes as a function of s. A first observation on the remanent states is that only two configurations (Rem X and Rem Y) can be obtained for $s \leq 200$ nm. Indeed, no 45° domains appear for H_0 applied at $\theta \approx 45°$. They are shown in Figs. 3(c)–3(e) for each value of s. The Rem Y and Rem X states appear for θ above or below 45°, respectively.

For $s = 200$ nm, the spin-wave modes in the Rem Y state are quite similar to the one obtained for the A4 state. However, the low-frequency confined-edge mode has become the most intense. Its attenuation in the Rem X configuration is still about −10 dB. The second most intense mode corresponds to the quasiuniform stripe mode and shows an attenuation of about −42 dB. As compared to the case $s = 300$ nm, we have also more modes with a relatively high intensity and attenuation better than −20 dB in the Rem X configuration. Therefore, this configuration gives more flexibility for reconfigurable operations.

When $s = 100$ or 50 nm, the magnetization in the central part of the unit cell is not fully aligned along the Y (X) direction for the Rem Y (Rem X) state [Figs. 3(d) and 3(e)]. This effect is even stronger for $s = 50$ nm. This is because edge domains aligned along the diagonal get closer from each other and start to spread in the central part of the unit cell. The direct consequence of a slight tilt of the averaged magnetization with respect to the X or Y axes has been addressed in Ref. [36] for circular antidot arrays made of Permalloy under a magnetic field applied at few degrees from the symmetry axes of the array. In their case, the authors have shown that low-frequency modes become a combination of asymmetric channel and edge mode (see Figs. 4 and 5 in Ref. [36]). Also, they observed that low-frequency modes show a maximum amplitude in the channel connecting opposite antidots in the diagonal direction. Even if in the present study we explore remanent states and a different material, our results for $s = 100$ and 50 are very similar to their conclusions. It can be seen in Figs. 3(d) and 3(e) that mode 1 does not correspond to a magnetic precession well localized in the edge domain. This is similar to the lowest-frequency mode described in Ref. [36]. Its frequency is still low, i.e., within the range observed for $s = 300$ or 200 nm, because it is driven by the edge domain where the effective field is
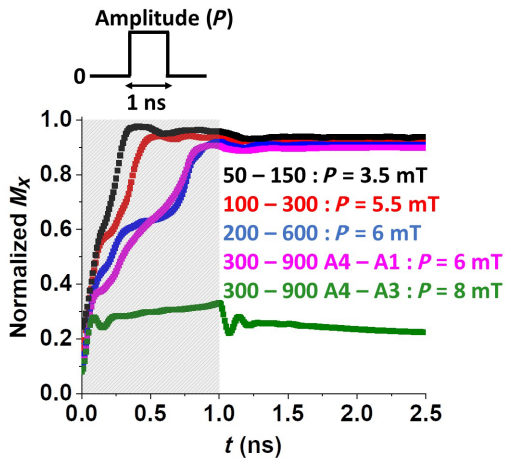
FIG. 4.   Simulations of the switching times between different equilibrium configurations. The black, red, and blue curves correspond to the transition from the Rem Y to Rem X states for $s = 50$, 100, and 200 nm, respectively. The violet and green curves correspond to the transition from the A4 to A1 and from A4 to A3 states, respectively. The aspect ratio is always $s/d = 1/3$. The duration of the magnetic field pulse is 1 ns and it is aligned along the X direction except for the A4 to A3 transition for which it is applied at 45° from the X axis.

small. For higher-frequency modes, our results are similar to the dragonfly modes observed in Ref. [36].

We also observe that the frequencies of higher-order modes increase as s decreases below 200 nm. This is expected. Indeed, the spatial confinement of the spin waves increases when reducing the distance between the antidots. This enhances the angle between neighboring precessing spins, leading to an additional contribution of the exchange interaction to the effective field and to the resonance frequency. Such an effect is somehow similar to the contribution of the exchange energy to the frequencies of quantized modes in stripes [37,38].

One of the main difference for $s = 100$ or 50 nm as compared to $s = 300$ or 200 nm is that the high-frequency modes show a relatively small amplitude with respect to the main one. However, reconfigurable operations can be achieved, as the microwave response between the Rem Y and Rem X states is different. For example, the attenuation for mode 2 for $s = 100$ or 50 nm is still around -30 dB while it reaches around -20 dB for the other modes. Then playing with the values of s, and possibly on the shape of the antidots other than squares, allows setting the working frequency of the device in the desired frequency range of application.

In order to go further in the potential of this device for microwave applications, we numerically test the required minimum amplitude for H_0 and the time to switch between the different configurations when $s/d = 1/3$. For $s = 300$ nm, we start from the A4 configuration and look at the switching time into the A1 or A3 states. For

$s \neq 300$ nm, we look at the switching from the Rem Y to the Rem X state. In order to compare with other studies, we apply the same methodology as described in Ref. [39]. To our knowledge, these authors were pioneering to explore such parameters in the case of devices devoted to magnonic applications. A magnetic field pulse is applied in the X direction, except for the transition between A4 and A3 for which the pulse is applied at 45° from the X axis. The pulse duration is 1 ns with an absolute amplitude P.

Results are shown in Fig. 4. For every value of s, switching is achieved within roughly 1 ns. Only the transition between A4 to A3 is achieved above 1 ns (approximately equal to 1.2 ns). Also, the field amplitude is of few mT and decreases with s. This is about one order of magnitude lower than in the case of the nano-objects made in Permalloy proposed in Refs. [16,17,39]. But it is worthwhile to mention that their system has been designed to achieve nanoscale integration, while our system is more relevant for micrometer-scale devices (see discussion below). As mentioned in Ref. [39], a simple scheme with two perpendicular current lines placed above the MC can achieve the switching mechanism. However, reaching such magnetic field amplitude with current lines is still energy consuming and further optimization of the device design must be driven to reduce it, such as with different shapes of antidots.

Now that we show the possibility of obtaining reconfigurable operations with a simple pseudoinfinite geometry, the question of the validity of our approach on a device with finite dimensions is raised. Indeed, for finite dimensions, flux closure magnetic domains at the edge of the sample will inevitably arise. We address this question by performing micromagnetic simulations with OOMMF on large samples. These simulations are performed with the high-performance computing (HPC) resources of the CALMIP supercomputing center. The evolver and driver used in the simulations of the remanent states are, respectively, "Oxs_CGEvolve" and "Oxs_mindriver." The convergence criteria is set to $m \times H \times m = 10$ and we verify that the results are the same for values down to 1.

Calculations are performed for an antidot lattice with $s = 300$ nm, $s/d = 1/3$. We test two geometries. In the first case, the spacing between the edge of the last antidot row (or column) and the edge of the sample is equal to 1/2 of the interdot distance, i.e., 450 nm. In the second case, the spacing is null. For the sake of clarity, Fig. 5 shows only the remanent states for H_0 applied along the X and Y directions and sample dimensions $14\,400 \times 14\,400 \times 20$ nm³ in the first case and $13\,500 \times 13\,500 \times 20$ nm³ in the second case. But the same magnetic states are obtained for samples from $9900 \times 9900 \times 20$ nm³ up to $29\,400 \times 29\,400 \times 20$ nm³.

For the first geometry [Fig. 5(a) and 5(b)], the magnetization at the right and at the left of the sample is aligned along the Y direction in the area between the edge of the
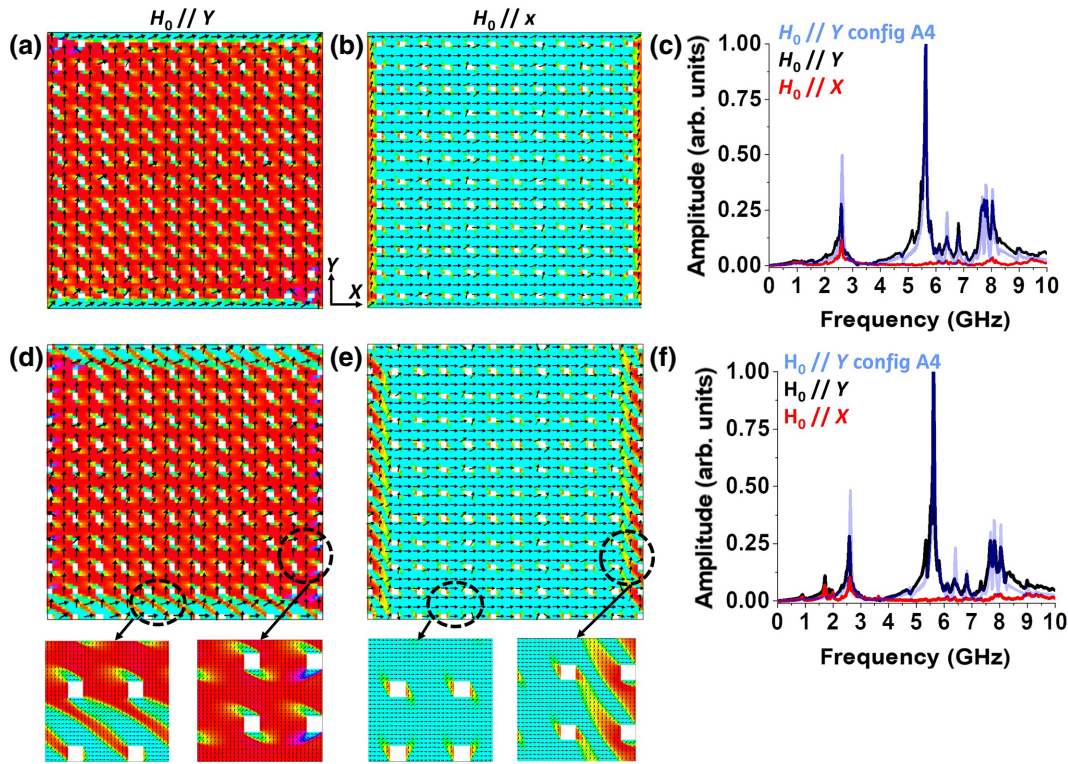
FIG. 5. Remanent states of a finite-size sample with lateral dimensions $14.4 \times 14.4 \ \mu m^2$ (a), (b) and $13.5 \times 13.5 \ \mu m^2$ (d), (e). The antidot lateral size is 300 nm and $s/d = 1/3$. The saturation field is applied parallel to the Y axis in (a), (d) and to the X axis in (b), (e). (c) FFT spectra for the remanent states presented in (a), (b). (f) FFT spectra for the remanent states presented in (d), (e). For comparison the FFT spectrum for the A4 configuration of Fig. 2(a) is shown in light blue in (c), (f).

sample and the first antidot column. At the top and bottom of the sample, the magnetization is aligned along X in the area between the edge of the sample and the first antidot row. We refer to these areas as uniform domains. Each of them has a width of 450 nm. It is worthwhile to mention that the magnetization in these areas is always aligned in the same direction either if H_0 is applied in the X or Y direction.

The areas at the left and right could potentially couple to h_{rf}. However, they represent a small portion of about 5% of the total magnetic volume (for this particular sample dimensions of about 14 μm). To verify their impact on the microwave response of the device, we calculate the FFT spectra as shown in Fig. 5(c). The results are very similar to those obtained for the A1 and A4 configurations in Fig. 2(a). For comparison, the FFT spectra of the A4 configuration is shown in light blue in Fig. 5(c). The main difference is a small enlargement of the resonance peaks with the apparition of a little satellite peak at 5.2 GHz close from the main mode, and a slight decrease of the relative amplitude of mode 3 while the one of mode 4 increases. The attenuation values are similar to the ones discussed above for the A1 and A4 states. As the size of the sample will increase, the FFT spectrum will be closer and closer from the ones of the pseudoinfinite case as the

influence of the magnetic nonuniformity will be reduced. We also verify that a sample with the same dimension with $s = 100$ nm, $s/d = 1/3$ shows a similar FFT spectrum as in the Rem X and Rem Y states presented in Fig. 3(d). Therefore, all results presented above for a pseudoinfinite geometry are valid and such a geometry is very well suited for applications.

In the second case presented in Figs. 5(d) and 5(e) the magnetic states are more nonuniform both on the lateral or vertical edges. Also, and oppositely to the first geometry tested, the magnetization on the edges varies as a function of the direction of H_0, as shown in the inset below the figures. For this sample size, the nonuniform magnetic areas represent about 17% of the total magnetic volume. The main difference with the microwave response in the A4 or A1 states of Fig. 2(a) is the apparition of a low-frequency mode around 1.8 GHz, and a decrease of the relative amplitude of the modes with frequencies above the main mode. Depending on the modes considered, the amplitude is decreased between 10 to 40%. Consequently, high-frequency modes show marred attenuations between -10 and -20 dB only in this geometry.

As a conclusion, the impact of flux closure magnetic domains that always form at remanence in finite-size devices can be reduced with a proper design of the MC

[such as the geometry of Fig. 5(a)] in addition to an increase of the lateral dimensions of the sample if needed.

V. PROPAGATION PROPERTIES OF MC WITH $s = 100$ nm AND $s/d = 1/3$

We now discuss the properties of our MC to propagate spin waves for filtering applications. In particular, we are interested in the possibility to obtain on-demand spin waves propagating in the MSSW or MSBVW configurations at remanence. In the case of MSSW in stripes, it is generally necessary to apply a bias field to stabilize the magnetization along the width of the stripe. Therefore, the possibility to use the strong cubic anisotropy to stabilize the magnetization without the need for bias field is particularly interesting. Also, spin-wave propagation in MC at remanence is rarely discussed in the literature. Most of the studies performed on the filtering properties of MC have been performed under bias field either for MSSW or MSBVW in order to avoid complex nonuniform magnetic states [40–43]. However, for filtering applications, it is of particular interest to propose MC working at remanence. In addition, materials such as Heusler alloys with low-damping coefficients offer the possibility to propagate spin waves over several microns.

We simulate the propagation of spin waves through 40 columns of antidots as shown in Fig. 6. This number of antidots is similar to other studies [44]. Due to limited computer resources, we test only a MC with $s = 100$ nm and $d = 300$ nm and we use periodic boundary conditions in the Y direction. The width of the filter is then 800 nm (160 cells). Periodic boundary conditions also allow avoiding the complications related to reflections on the top and bottom edges of the waveguide [45,46]. The full length of the waveguide is 61.44 μm long (12 288 cells). On each side of the MC, we have two areas of unpatterned Co$_2$MnSi with a length of 22 microns each. At both ends of the waveguide, the damping is linearly increased up to 0.1 over a distance of 5 microns. This ensures reflexions of spin waves on the edge of the sample are avoided, which might perturb the analysis of the filtering properties.

We test two geometries for the microwave excitation. In case 1, the rf pulse is located at a distance $L = -7$ μm from the first unit cell of the MC as shown in Fig. 6(a). In case 2, it is located at the center of the MC ($L = 16$ μm). In case 2, we simulate a MC with 80 columns to study the propagation within 40 columns such as in case 1. We excite the magnetization with a Sinc function as describes above. The field is applied on one column of cells, therefore on a width of 5 nm, giving a cutoff spatial frequency of 1.256 rad/nm. The field pulse is applied either in the X or Z direction for MSSW or MSBVW excitation, respectively. To observe the frequency-filtering properties and propagation of spin waves, we calculate the FFT spectrum for each cell along the X direction over a length of more than 20 μm. For case

1, this ensures the MC is surrounded and both the antenna region and the output region after the MC are observed. Also, the spectra are averaged on the 160 cells in the Y direction. The results are shown as $f(x)$ diagrams.

The $f(x)$ diagrams are compared to spin-wave dispersion curves $f(k_x)$ obtained from a 2D FFT treatment performed on an infinite MC. To obtain the dispersion curves, we record for a duration of 40.96 ns every 10 ps (Nyquist frequency 50 GHz, resolution approximately equal to 25 MHz) the temporal evolution of the dynamic $M_z(\tau)$ component in a MC made of 4160 cells along X and 160 cells along Y and using 2D PBC. The microwave pulse is located on one column of cells at the center of the MC. The pulse is a Sinc function with a cutoff frequency of 30 GHz. The $f(k_x)$ curves are obtained after subtraction of the remanent state to each temporal $M_z(\tau)$ file, followed by a 2D FFT performed on the 4096 temporal files and 4096 cells along X. This gives a resolution of 3×10^{-4} rad/nm for k_x. Also, the 2D FFT are averaged over the 160 cells along the Y direction.

Let us note that the full understanding of the spin-wave modes allowing propagation through the magnonic crystal implies a careful analysis as performed in the very complete work of Semenova and Berkov [42] in the case of MSFVW. They demonstrated that the understanding of the spin-wave propagation through the MC implies a detailed analysis of the spatial symmetry of the different modes of the MC. Such analysis falls beyond the scope of the present paper whose aim is mainly to demonstrate the potential of our device for magnonic filtering properties at remanence. However, general considerations can be done to understand the main feature of filtering properties.

We begin by studying the propagation of MSSW modes. The results are presented in Fig. 7. In this case, the magnetization is uniformly magnetized along the Y direction in the unpatterned part beside the MC, and the configuration is similar to the Rem Y state in Fig. 3(c), except for the last columns of antidot at the boundaries with the unpatterned part as shown in Fig. 6(b). We focus our attention on the band 2.5–14 GHz for which filtering properties can be observed. Indeed, for frequencies above, the modes excited in the MC by the incoming waves vanish before they can exit the MC.

The observation of the $f(k_x)$ diagram on infinite MC shows a very rich structure. We present here only the two first Brillouin zones (first BZ = $\pi/400$ nm). In order to compare with a simple geometry, we superpose in the diagram the dispersion curves of the first MSSW ($n = 1$) mode in a waveguide of 280 nm (dark) and 130 nm (dotted red) based on the formula of Kalinikos et al. [47–49]. The first width value corresponds to the area between the dots excluding the very small zone close from the edge of the antidot where the magnetization is almost parallel to the X direction [see Fig. 6(b)]. The second value corresponds to the area between the boundaries of the edge domains. Also,
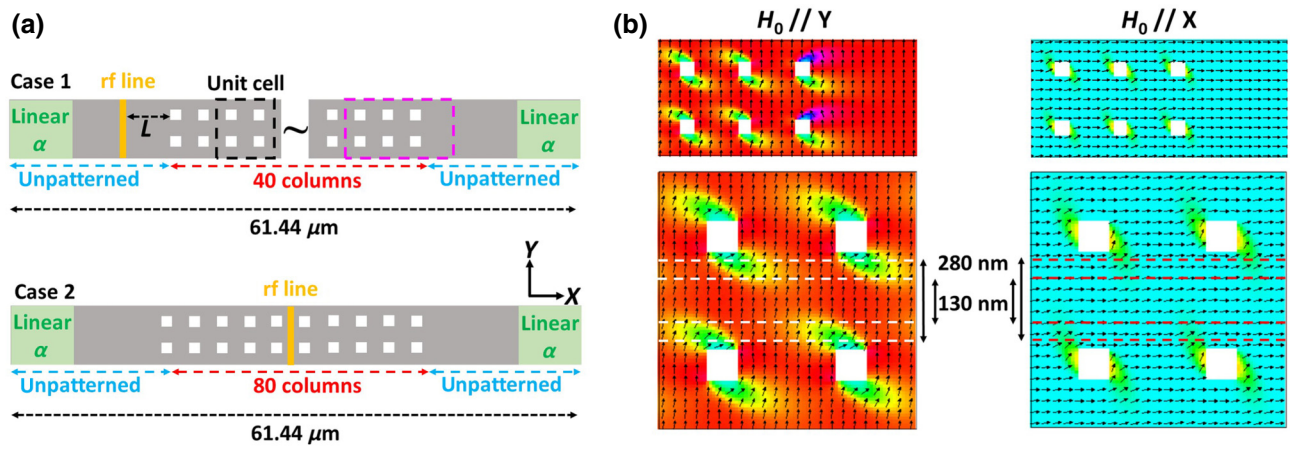
FIG. 6.   (a) Schematic of the two configurations tested for spin-wave propagation through the MC. In case 1, the rf excitation line is before the MC, in the unpatterned Co_2MnSi part. In case 2, the excitation is in the middle of the MC. The green part on each side of the filter shows the area where the damping is linearly increased from 0.001 to 0.1. The length of these areas is 5 microns. (b) (Top) Remanent configuration for the last unit cell at the boundary with the unpatterned part for a saturation field applied along Y (left) or X (right), as shown by the violet box in (a). (Bottom) Enlargement of one unit cell in the Rem Y (left) and Rem X (right) configurations. The internal dotted lines delimit an area of width 130 nm between the edge domains where the magnetization is almost uniformly aligned. The external dotted lines delimit an area of width 280 nm for which the magnetization is always oriented with an angle above (left) or below (right) 45° from the X axis.

on the right of the $f(k_x)$ diagram, we show for comparison the frequency position and spatial profile of the modes obtained in Fig. 3(d) for a uniform microwave excitation (i.e., $k = 0$ rad/nm).

We first observe two low-frequency propagating bands between 3.3 and 5.1 GHz. These bands appear at a frequency close to the one of mode 1 in Fig. 3(d), meaning that the propagation of spin waves is most probably driven by the dipolar coupling between the edge domains. Two other propagative bands appear between 5.8 and 7.7 GHz. We can see that the two dispersion curves calculated for waveguides of 280 and 130 nm fit these bands reasonably well. This shows that the $f(k_x)$ diagram is most probably composed of multiple modes related to different spatial confinement because of the nonuniform magnetization configuration inside of the MC. For frequencies between 8 and 12 GHz, the band diagram is even more complex. This is expected as a high number of stationary modes is already observed for a uniform excitation in Fig. 3(d). Also, magnetic inhomogeneities, especially in the edge domain where the magnetization is not aligned with the Y axis, might be the source of hybridization between MSSW and spin waves propagating with a canted angle. All of these phenomena lead to a very rich and complex band diagram.

We now look at the $f(x)$ curves in case 1 of Fig. 6(a). The first observation is the interference pattern, which appears at the left of the MC in Fig. 7(a) because of the reflexion of the spin waves at the boundary with the MC [42]. After the MC, we observe basically three principal band gaps in the transmission frequency pattern, which are

highlighted by the violet boxes. These gaps are numbered 2, 3, and 4. For gaps 2 and 4, they appear in a frequency range where spin-wave modes in the MC show very small group velocities, i.e., the dispersion curve is almost flat (as can be seen, for example, with the modes around 8 GHz and $k_x = 5 \times 10^{-3}$ rad/nm). Then we assume that incoming waves weakly couple to these modes. Also, we can see on Fig. 7(a) that they vanish in the MC after few microns. The width of the frequency gaps are about 1 and 0.7 GHz, respectively. Gap 3 seems to correspond to the destructive interference of the waves in the 280-nm pseudowaveguide at the first BZ. The gap is quite small around 0.3 GHz.

Finally, we observe that gap 1 does not exist. This is because the FMR mode in the unpatterned part appears around 6 GHz, and then no incoming modes can couple to the 3.3–5.1 GHz propagating band of the MC. However, it is interesting to see that the mode at 3.3 GHz is excited inside the MC. We are not able to explain such an observation at this stage and further numerical studies are required to understand fully its origin. Our assumption is that it might be related to the relaxation of high-frequency modes toward the lowest-frequency mode, similarly to the processes described in the formation of Bose-Einstein magnons' condensate [50,51]. Nevertheless, such an effect requires microwave power higher than in the present work. Therefore, numerical studies at different frequencies and microwave powers would be interesting to probe the physical mechanisms behind the excitation of the low-frequency mode. But this is beyond the scope of the present paper.

In case 2 of Fig. 6(a), the excitation antenna is located at the center of the MC and propagating spin waves in the
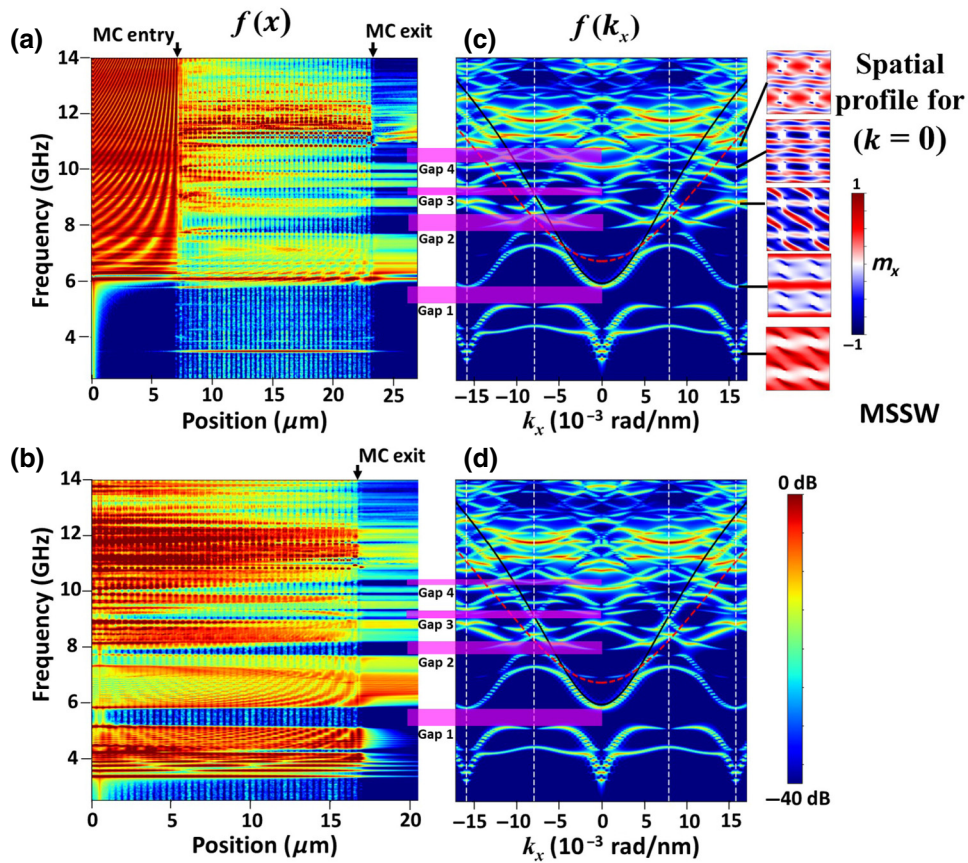
FIG. 7.   (a), (b) Amplitude of spin waves at remanence as a function of frequency and position along the MC. The position of the excitation antenna corresponds to case 1 (a) and 2 (b) described in Fig. 6(a). The saturation field is applied in the Y direction. (c), (d) Amplitude of spin waves as a function of frequency and wave vector k_x in the case of an infinite MC in the Rem Y state. The amplitude in the $f(x)$ and $f(k_x)$ spectra is calculated on the dynamic m_z component and are color coded following the color bar on the right of (d). A -40-dB scale is applied for all spectra. The black and dotted red lines correspond to the dispersion curves calculated for MSSW in a waveguide of 280 and 130 nm, respectively. White dotted vertical lines mark the two first BZs. Beside (c) we show the snapshots of the m_x dynamic component in a unit cell obtained for a uniform microwave excitation ($k = 0$) applied in the X direction. The frequencies of these modes are shown by the dark lines and correspond to the bottom of the different propagating bands.

3.3–5.1 GHz frequency band can be excited. However, as there are no corresponding frequencies in the unpatterned part, these modes vanish very quickly at the exit of the MC and stay mainly confined in the MC. The width of gap 1 in the MC is about 0.7 GHz. For frequencies above 5.1 GHz, we recover similar features as in case 1. However, two main differences are observed. First, the width of gaps 2 and 4 are smaller (0.4 and 0.3 GHz, respectively). One possible explanation is that more energy is given to the modes with low group velocities when the antenna is within the MC. In case 1, most of the incoming energy is reflected at the entry of the MC. In case 2, the modes do not fully vanish before they can exit the system and then the gap is reduced. This is particularly visible for gap 2 for frequencies between 8 and 8.4 GHz. The other difference is that gap 3 disappears in case 2. The reason for such an effect is not clear and further numerical analysis will

be necessary to understand this point. It may be related to the local modification of the magnetic configuration in the edge domains at the border of the crystal, as shown in Fig. 6(b). This can change locally the dispersion curve of spin waves with respect to the case of infinite crystal, allowing the coupling of modes between the exit of the MC and the unpatterned area. A deeper insight into the local spin-wave excitation on the edge of the MC is required to validate this assumption.

We now turn to the study of the propagation of MSBVW. In order to compare with the case of MSSW, we simulate the propagation through the same number of columns. Simulations are performed with the magnetization first saturated along the X direction. Therefore, the magnetization is parallel to the X axis in the unpatterned part and shows the Rem X configuration of Fig. 3(d) inside the MC. The $f(k_x)$ diagram is shown up to 9 BZ in order to observe
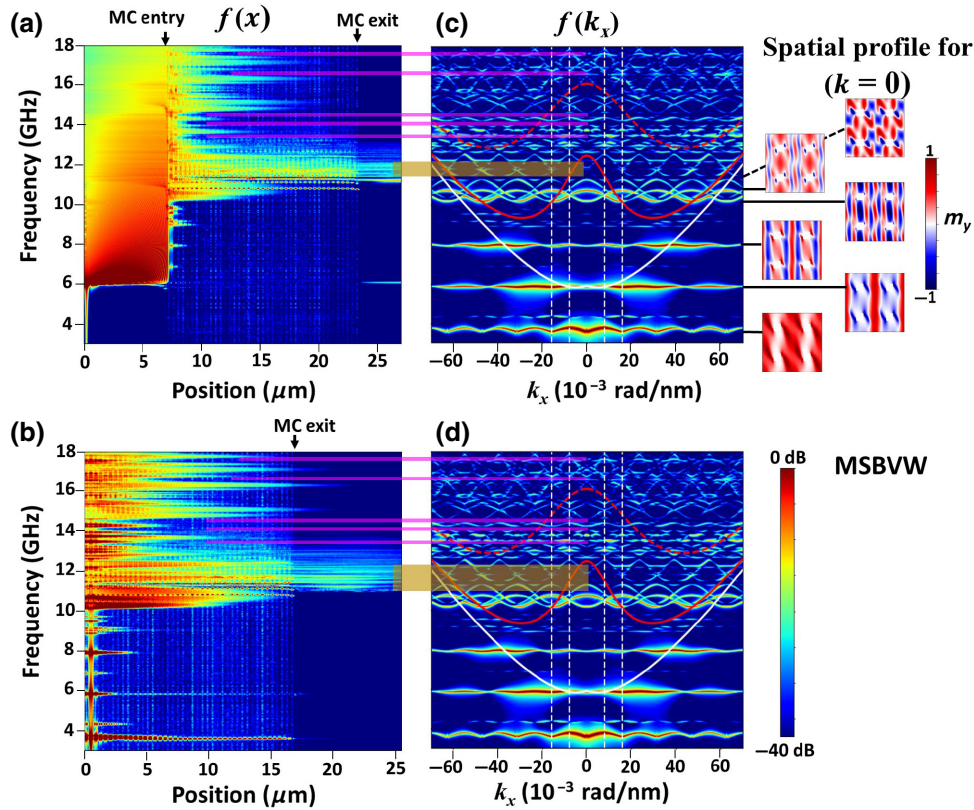
FIG. 8. (a), (b) Amplitude of spin waves at remanence as a function of frequency and position along the MC. The position of the excitation antenna corresponds to case 1 (a) and 2 (b) described in Fig. 6(a). The saturation field is applied in the X direction. (c), (d) Amplitude of spin waves as a function of frequency and wave vector k_x in the case of an infinite MC in the Rem X state. The amplitude in the $f(x)$ and $f(k_x)$ spectra are calculated on the dynamic m_z component and are color coded following the color bar on the right of (d). A -40-dB scale is applied for all spectra. The white, full red, and dotted red lines correspond to the dispersion curves calculated for MSBVW in an infinite thin film, a waveguide of 280 and 130 nm, respectively. White dotted vertical lines mark the first two BZs. Beside (c) we show the snapshots of the spatial profile of the m_y dynamic component in a unit cell obtained for a uniform microwave excitation ($k = 0$) applied in the Z direction. The frequencies of these modes are shown by the dark lines and correspond to the bottom of the different propagating bands or to the frequencies of the quasistationary modes.

the characteristic well shape of the dispersion curve in the MSBVW configuration. We superpose in white the dispersion curve of the infinite film, in full red and dotted red lines the first ($n = 1$) MSBVW modes in a waveguide with a width of 280 and 130 nm, respectively. These values are similar to the ones in the MSSW configuration as the Rem X and Rem Y configurations are similar via a 90° rotation. On the right, we show the spatial profile of the dynamic m_y component obtained for a uniform microwave excitation in the Rem X state, with the direction of the field pulse in the Z direction.

We begin with case 1 for which the antenna is located before the MC. As shown by the green box in Fig. 8(a), spin waves are recovered after the MC only in a single frequency band of about 0.8 GHz centered around 11.5 GHz. We assume that it corresponds to spin waves with high k_x values and then positive group velocities, propagating in the horizontal channel between antidots. This assumption

is supported by the good agreement between the calculated dispersion curve in a waveguide with a width of 280 nm and the one of the MC at high k_x values (see, for example, the modes around 12 GHz and $k_x \approx 60 \times 10^{-3}$ rad/nm). Also, no real band gap is observed after the MC and other modes excited in the MC by the incoming waves vanish after few microns only. In the MC, we can see some very small gaps (shown by the violet boxes), each of them being about 0.2 GHz. The first, fourth, and fifth gaps correspond to the excitation of quasistationary modes (i.e., with group velocities almost null on the full k_x range) in the MC while the second and third gaps appear between the top and bottom of the propagative bands. From an application point of view, it is necessary to reduce the number of rows to benefit from these band gaps. Other features can be observed in the $f(x)$ diagram. While the modes around 3.6 GHz cannot be excited by MSBVW coming from the unpatterned part, the modes around 5.8 and 7.9 GHz are barely excited, or

only over very small distance of 1 or 2 microns because of their very small group velocities that tend to confine these modes locally.

Similar features are observed in the case where the microwave excitation is located inside the MC. Such as for the MSSW configuration, the lowest frequency modes are excited but cannot exit the MC. We recover again the small propagation distance of the modes around 5.8 and 7.9 GHz and the frequency band (green box) at the output of the MC. This band is slightly larger than in the previous case (approximately equal to1.1 GHz). For higher frequencies, we observe few modes around 16.5 GHz with high group velocities, which are able to exit the MC and propagate in the unpattern film over few microns.

VI. CONCLUSION

In conclusion, we study the possibilities offered by strong cubic anisotropy materials with low-damping coefficient such as Co_2MnSi alloy to obtain multiple remanent magnetic states and reconfigurable microwave responses to a dynamic excitation. While the results presented here are obtained for quasi-infinite magnonic crystals, we show that they are consistent for systems with dimensions of few microns. The diversity of magnetic states and microwave responses obtained as a function of the dimensions of the artificial pattern and its orientation with respect to the crystal anisotropy axes opens up interesting perspectives for microwave devices such as filters. Our devices can achieve amplitude attenuation at particular frequencies with reconfigurable magnetic states obtained on a time scale below 1 ns with relatively low initialization magnetic fields. Such devices also offer the possibility to filter particular spin-wave frequency bands at remanence, which is of particular interest for the future generation of spin-wave-based applications such as data processing or neuromorphic computing [52].

ACKNOWLEDGMENTS

[1] A. V. Chumak, V. I. Vasyuchka, A. A. Serga, and B. Hillebrands, Magnon spintronics, Nat. Phys. **11,** 453 (2015).

[2] A. V. Chumak, A. A. Serga, and B. Hillebrands, Magnonic crystals for data processing, J. Phys. D: Appl. Phys. **50,** 244001 (2017).

[3] Q. Wang, P. Pirro, R. Verba, A. Slavin, B. Hillebrands, and A. V. Chumak, Reconfigurable nanoscale spin-wave directional coupler, Sci. Adv. **4,** e1701517 (2018).

[4] A. V. Chumak, V. I. Vasyuchka, A. A. Serga, M. P. Kostylev, V. S. Tiberkevich, and B. Hillebrands, Storage-Recovery Phenomenon in Magnonic Crystal, Phys. Rev. Lett. **108,** 257207 (2012).

[5] A. V. Chumak and H. Schultheiss, Magnonics: Spin waves connecting charges, spins and photons, J. Phys. D: Appl. Phys. **50,** 300201 (2017).

[6] A. V. Chumak, A. A. Serga, and B. Hillebrands, Magnon transistor for all-magnon data processing, Nat. Commun. **5,** 4700 (2014).

[7] J. Topp, D. Heitmann, M. P. Kostylev, and D. Grundler, Making a Reconfigurable Artificial Crystal by Ordering Bistable Magnetic Nanowires, Phys. Rev. Lett. **104,** 207205 (2010).

[8] R. Verba, G. Melkov, V. Tiberkevich, and A. Slavin, Fast switching of a ground state of a reconfigurable array of magnetic nano-dots, Appl. Phys. Lett. **100,** 192412 (2012).

[9] J. Ding, M. Kostylev, and A. O. Adeyeye, Realization of a mesoscopic reprogrammable magnetic logic based on a nanoscale reconfigurable magnonic crystal, Appl. Phys. Lett. **100,** 073114 (2012).

[10] A. V. Chumak, T. Neumann, A. A. Serga, B. Hillebrands, and M. P. Kostylev, A current-controlled, dynamic magnonic crystal, J. Phys. D: Appl. Phys. **42,** 205005 (2009).

[11] M. Vogel, A. V. Chumak, E. H. Waller, T. Langner, V. I. Vasyuchka, B. Hillebrands, and G. von Freymann, Optically reconfigurable magnetic materials, Nat. Phys. **11,** 487 (2015).

[12] E. Albisetti, D. Petti, M. Pancaldi, M. Madami, S. Tacchi, J. Curtis, W. P. King, A. Papp, G. Csaba, W. Porod, P. Vavassori, E. Riedo, and R. Bertacco, Nanopatterning reconfigurable magnetic landscapes via thermally assisted scanning probe lithography, Nat. Nanotechnol. **11,** 545 (2016).

[13] J. C. Gartside, A. Vanstone, T. Dion, K. D. Stenning, D. M. Arroo, H. Kurebayashi, and W. R. Branford, Reconfigurable magnonic mode-hybridisation and spectral control in a bicomponent artificial spin ice, Nat. Commun. **12,** 2488 (2021).

[14] H. Merbouche, I. Boventer, V. Haspot, S. Fusil, V. Garcia, D. Gouéré, C. Carrétéro, A. Vecchiola, R. Lebrun, P. Bortolotti, L. Vila, M. Bibes, A. Barthélémy, and A. Anane, Voltage-controlled reconfigurable magnonic crystal at the sub-micrometer scale, ACS Nano **15,** 9775 (2021).

[15] A. Haldar and A. O. Adeyeye, Reconfigurable and self-biased magnonic metamaterials, J. Appl. Phys. **128,** 240902 (2020).

[16] K. Begari and A. Haldar, Reconfigurable microwave properties in trapezoid-shaped nanomagnets without bias magnetic field, J. Magn. Magn. Mater. **540,** 168431 (2021).

[17] K. Begari and A. Haldar, Reconfigurable microwave properties in C-, L- and S-shaped nanomagnets, J. Phys. D: Appl. Phys. **52,** 335003 (2019).

[18] P. J. Brown, K. U. Neumann, P. J. Webster, and K. R. A. Ziebeck, The magnetization distributions in some Heusler alloys proposed as half-metallic ferromagnets, J. Phys.: Condens. Matter **12,** 1827 (2000).

[19] I. Abdallah, B. Pradines, N. Ratel-Ramond, G. BenAssayag, R. Arras, L. Calmels, J. F. Bobo, E. Snoeck, and N. Biziere, Evolution of magnetic properties and damping coefficient of Co2 MnSi Heusler alloy with Mn/Si and Co/Mn atomic disorder, J. Phys. D: Appl. Phys. **50,** 035003 (2017).

[20] I. Abdallah, N. Ratel-Ramond, C. Magen, B. Pecassou, R. Cours, A. Arnoult, M. Respaud, J. F. Bobo, G. BenAssayag, E. Snoeck, and N. Biziere, Structural and magnetic properties of He$^+$ irradiated Co2 MnSi Heusler alloys, Mater. Res. Express **3**, 046101 (2016).

[21] T. Graf, C. Felser, and S. S. P. Parkin, Simple rules for the understanding of Heusler compounds, Prog. Solid State Chem. **39**, 1 (2011).

[22] C. Guillemard, S. Petit-Watelot, J.-C. Rojas-Sánchez, J. Hohlfeld, J. Ghanbaja, A. Bataille, P. Le Fèvre, F. Bertran, and S. Andrieu, Polycrystalline Co2 Mn-based Heusler thin films with high spin polarization and low magnetic damping, Appl. Phys. Lett. **115**, 172401 (2019).

[23] S. Andrieu, A. Neggache, T. Hauet, T. Devolder, A. Hallal, M. Chshiev, A. M. Bataille, P. Le Fèvre, and F. Bertran, Direct evidence for minority spin gap in the *Co2MnSi* Heusler compound, Phys. Rev. B **93**, 094417 (2016).

[24] M. Jourdan, J. Minár, J. Braun, A. Kronenberg, S. Chadov, B. Balke, A. Gloskovskii, M. Kolbe, H. J. Elmers, G. Schönhense, H. Ebert, C. Felser, and M. Kläui, Direct observation of half-metallicity in the heusler compound *Co2MnSi*, Nat. Commun. **5**, 3974 (2014).

[25] C. Guillemard, S. Petit-Watelot, T. Devolder, L. Pasquier, P. Boulet, S. Migot, J. Ghanbaja, F. Bertran, and S. Andrieu, Issues in growing Heusler compounds in thin films for spintronic applications, J. Appl. Phys. **128**, 241102 (2020).

[26] J. Létang, C. de Melo, C. Guillemard, A. Vecchiola, D. Rontani, S. Petit-Watelot, M.-W. Yoo, T. Devolder, K. Bouzehouane, V. Cros, S. Andrieu, and J.-V. Kim, Nanocontact vortex oscillators based on Co$_2$ MnGe pseudo spin valves, Phys. Rev. B **103**, 224424 (2021).

[27] C. Felser and A. Hirohata, *Heusler Alloys: Properties, Growth, Applications* (Springer International Publishing, Switzerland, 2016).

[28] F. Casper, T. Graf, S. Chadov, B. Balke, and C. Felser, Half-Heusler compounds: Novel materials for energy and spintronic applications, Semicond. Sci. Technol. **27**, 063001 (2012).

[29] C. Felser, L. Wollmann, S. Chadov, G. H. Fecher, and S. S. P. Parkin, Basics and prospective of magnetic Heusler compounds, APL Mater. **3**, 041518 (2015).

[30] A. Vansteenkiste, J. Leliaert, M. Dvornik, M. Helsen, F. Garcia-Sanchez, and B. Van Waeyenberge, The design and verification of MuMax3, AIP Adv. **4**, 107133 (2014).

[31] C. Guillemard, S. Petit-Watelot, L. Pasquier, D. Pierre, J. Ghanbaja, J.-C. Rojas-Sánchez, A. Bataille, J. Rault, P. Le Fèvre, F. Bertran, and S. Andrieu, Ultralow Magnetic Damping in Co2 Mn-Based Heusler Compounds: Promising Materials for Spintronics, Phys. Rev. Appl. **11**, 064009 (2019).

[32] *Spin Dynamics in Confined Magnetic Structures I*, edited by B. Hillebrands and K. Ounadjela (Springer, Berlin, New York, 2002).

[33] *Spin Dynamics in Confined Magnetic Structures III*, edited by B. Hillebrands and A. Thiaville (Springer, Berlin, New York, 2006).

[34] H. Suhl, The theory of ferromagnetic resonance at high signal powers, J. Phys. Chem. Solids **1**, 209 (1957).

[35] P. W. Anderson and H. Suhl, Instability in the motion of ferromagnets at high microwave power levels, Phys. Rev. **100**, 1788 (1955).

[36] F. Groß, M. Zelent, A. Gangwar, S. Mamica, P. Gruszecki, M. Werner, G. Schütz, M. Weigand, E. J. Goering, C. H. Back, M. Krawczyk, and J. Gräfe, Phase resolved observation of spin wave modes in antidot lattices, Appl. Phys. Lett. **118**, 232403 (2021).

[37] C. Bayer, J. Jorzick, S. O. Demokritov, A. N. Slavin, K. Y. Guslienko, D. V. Berkov, N. L. Gorn, M. P. Kostylev, and B. Hillebrands, in *Spin-Wave Excitations in Finite Rectangular Elements,* in *Spin Dynamics in Confined Magnetic Structures III*, edited by B. Hillebrands and A. Thiaville (Springer, Berlin, Heidelberg, 2006), pp. 57–103.

[38] A. N. Slavin, S. O. Demokritov, and B. Hillebrands, in *Nonlinear Spinwaves in One- and Two-Dimensional Magnetic Waveguides,* in *Spin Dynamics in Confined Magnetic Structures I*, edited by B. Hillebrands and K. Ounadjela (Springer Berlin Heidelberg, Berlin, Heidelberg, 2002), Vol. 83, pp. 35–64.

[39] K. Begari and A. Haldar, Reconfigurable microwave properties of zigzag magnetic nanowires, J. Phys. D: Appl. Phys. **53**, 455005 (2020).

[40] S. Pan, J. W. Kłos, S. Mieszczak, A. Barman, and M. Krawczyk, Spin waves in periodic antidot waveguide of complex base, J. Phys. D: Appl. Phys. **50**, 275003 (2017).

[41] J. W. Kłos, D. Kumar, M. Krawczyk, and A. Barman, Influence of structural changes in a periodic antidot waveguide on the spin-wave spectra, Phys. Rev. B **89**, 014406 (2014).

[42] E. K. Semenova and D. V. Berkov, Spin wave propagation through an antidot lattice and a concept of a tunable magnonic filter, J. Appl. Phys. **114**, 013905 (2013).

[43] J. W. Kłos, D. Kumar, M. Krawczyk, and A. Barman, Magnonic band engineering by intrinsic and extrinsic mirror symmetry breaking in antidot spin-wave waveguides, Sci. Rep. **3**, 2444 (2013).

[44] Q. Wang, A. V. Chumak, L. Jin, H. Zhang, B. Hillebrands, and Z. Zhong, Voltage-controlled nanoscale reconfigurable magnonic crystal, Phys. Rev. B **95**, 134433 (2017).

[45] V. E. Demidov, S. O. Demokritov, K. Rott, P. Krzysteczko, and G. Reiss, Self-focusing of spin waves in permalloy microstripes, Appl. Phys. Lett. **91**, 252504 (2007).

[46] V. E. Demidov, S. O. Demokritov, K. Rott, P. Krzysteczko, and G. Reiss, Mode interference and periodic self-focusing of spin waves in permalloy microstripes, Phys. Rev. B **77**, 064406 (2008).

[47] B. A. Kalinikos, M. P. Kostylev, N. V. Kozhus, and A. N. Slavin, The dipole-exchange spin wave spectrum for anisotropic ferromagnetic films with mixed exchange boundary conditions, J. Phys.: Condens. Matter **2**, 9861 (1990).

[48] B. A. Kalinikos and A. N. Slavin, Theory of dipole-exchange spin wave spectrum for ferromagnetic films with mixed exchange boundary conditions, J. Phys. C: Solid State Phys. **19**, 7013 (1986).

[49] A. Mahmoud, F. Ciubotaru, F. Vanderveken, A. V. Chumak, S. Hamdioui, C. Adelmann, and S. Cotofana, Introduction to spin wave computing, J. Appl. Phys. **128**, 161101 (2020).

[50] S. O. Demokritov, V. E. Demidov, O. Dzyapko, G. A. Melkov, A. A. Serga, B. Hillebrands, and A. N. Slavin,

Bose–Einstein condensation of quasi-equilibrium magnons at room temperature under pumping, Nature **443,** 430 (2006).

[51] V. E. Demidov, O. Dzyapko, S. O. Demokritov, G. A. Melkov, and A. N. Slavin, Thermalization of a Para-metrically Driven Magnon Gas Leading to Bose–Einstein Condensation, Phys. Rev. Lett. **99,** 037205 (2007).

[52] J. Grollier, D. Querlioz, K. Y. Camsari, K. Everschor-Sitte, S. Fukami, and M. D. Stiles, Neuromorphic spintronics, Nat. Electron. **3,** 360 (2020).